RSC Advances

ROYAL SOCIETY OF CHEMISTRY

PAPER

View Article Online
View Journal | View Issue

Cite this: *RSC Adv.*, 2025, **15**, 17420

Unveiling 2D $Rb_3Bi_2I_6Cl_3$ and $Rb_3Bi_2I_3Cl_6$ perovskites for optoelectronic, solar cell and photocatalytic applications

Shahid Mehmood, *[a] Zahid Ali, *[a] Shah Rukh Khan,[a] Meznah M. Alanazi,[b] Shaimaa A M Abdelmohsen[b] and Mohamed Mousa *[c]

The removal of harmful lead from perovskite materials has led to a surge in interest in lead-free perovskite-based solar cells. Using density-functional theory (DFT) and a numerical simulation method using the solar cell capacitance simulator SCAPS-1D. This work aims to advance the field of lead-free perovskite solar cells by conducting a comparative analysis of lead-free perovskite materials. WIEN2k is employed to explore the structural, electronic and optical properties of the two dimensional (2D) halide perovskites $Rb_3Bi_2I_6Cl_3$ and $Rb_3Bi_2I_3Cl_6$, while their solar cell (SC) efficiency is estimated using SCAPS-1D. The reported structural properties are aligned with the experimental values. The electronic properties of $Rb_3Bi_2I_6Cl_3$ and $Rb_3Bi_2I_3Cl_6$ reveal their direct band gap semiconducting nature with band gaps of 2.02 and 1.99 eV, respectively. Their optical properties reveal that the compounds are activated under visible light, making them ideal for optoelectronic device and SC applications. To model the efficiency of these compound-based solar cells, MoO_3 is optimized as an electron transport layer (ETL); TiO_2–SnS_2 is optimized as a hole transport layer (HTL), and the respective thickness of the ETL, HTL and absorber are optimized as 180, 150 and 900 nm, respectively. $Rb_3Bi_2I_6Cl_3$ and $Rb_3Bi_2I_3Cl_6$ are used as the absorber layer (AL). Optimized solar cell devices based on FTO/TiO_2–SnO_2/$Rb_3Bi_2I_6Cl_3$ and $Rb_3Bi_2I_3Cl_6$/MoO_3/Ni achieved short-circuit current densities of 9.02 and 10.11 mA cm^{-2}, open-circuit voltages of 1.41 and 1.35 V, fill factors of 84.69% and 83.93%, and power conversion efficiencies (PCE) of 11.39% and 11.52%, respectively. Additionally, photocatalytic analysis demonstrates that all of the materials can evolve H_2 from H^+ and O_2 from H_2O/O_2. Additionally, the compound under study can reduce CO_2 to produce HCOOH, CO, HCHO, CH_4OH and CH_4. Based on these findings, 2D perovskites could be used in optoelectronic devices, photovoltaics, and photocatalysis—especially for water splitting and CO_2 reduction driven by visible light. These results facilitate future studies aimed at developing fully inorganic lead-free perovskite-based photovoltaics and photocatalysts.

Received 3rd April 2025
Accepted 7th May 2025

DOI: 10.1039/d5ra02328a

rsc.li/rsc-advances

1. Introduction

The rapid acceleration of commercialization and industrialization is leading to an increase in the use of power and energy.[1] There is an increasing concern that the persistent use of traditional fuels, including oils, hydrocarbon gas, natural gas and fossil fuels, has significant environmental impact associated with their uses, prompting studies on alternative energy sources.[2–4] A more sustainable approach to meet the growing energy demand and replacing non-renewable energy resources is urgently required through the efficient use of renewable energy sources.[5,6] The most capable renewable energy sources includes solar, wind, geothermal, hydro, ocean, bio, and tidal energy. The declining cost of solar cells (SCs) has led to a dramatic expansion in their manufacture in recent years. SCs have the potential to become a significant energy source, but they need to be affordable if they are to compete with fossil fuels. A strategy for the innovative generation of perovskite solar cells (PSCs) has been developed, demonstrating adequate performances to facilitate commercialization, after significant efforts to generate innovative cell materials. PSCs' potential to compete with natural gas, along with their cheap raw materials and easy manufacturing procedure, suggests they will have a significant influence on the SC industry.[7]

Organic, inorganic PSCs have recently swept the solar research field owing to their exceptional and excellent properties, which include an improved dielectric constant, low atomic energy, high electron mobility, low-temperature deposition, high hole mobility, appropriate manufacturing cost and high

[a]Department of Physics, University of Malakand Chakdara, Dir 18800, Pakistan. E-mail: shahiduom07@gmail.com; zahidf82@gmail.com
[b]Department of Physics, Collage of Science, Princess Nourah Bint Abdulrahman University, P.O. Box 84428, Riyadh, 11671, Saudi Arabia
[c]Electrical Engineering Department, Future University in Egypt, Cairo 11835, Egypt. E-mail: Mohamed.Moussa@fue.edu.eg

absorption compared with conventional silicon based SCs.[8,9] Recently, remarkable advancement in the effectiveness and constancy of PSCs have emerged as formidable contributors in the photovoltaic industry.[10–12] For example, in only a decade, PSCs went from an unstable 3% effectiveness to a stable 32% efficiency (η).[13]

Thin-film PSC technology has advanced due to simplified fabrication processes, adjustable energy gaps, and PCE exceeding 30% in lead (Pb) based organic/inorganic halide PSCs.[14] Despite these accomplishments, the presence of developing contaminants, specifically Pb, which induces toxicity, remains a central issue in the application of Pb based PSCs. This challenge continues to pose a substantial obstacle to the commercialization of PSCs.[15] The inclusion of organic elements in the perovskite layer (PL) contributes to the instability of the SC. Consequently, Pb based organic halide PSCs are unsuitable and not preferred for industrial applications and commercialization. Nonetheless, challenges such as Pb toxicity and concerns regarding stability impede the practical application of the perovskites, making it essential to explore lead-free alternatives. These substitutes must exhibit outstanding optoelectronic properties, affordability, and straightforward recyclability. Alongside the challenge of competing with current PV technologies, there is also a necessity to meet commercial demands such as scalability, consistency and flexibility.[15–17] Researchers have conducted experiments to develop Pb free perovskite materials to eliminate toxicity and reduce instability. The use of inorganic materials has garnered significant consideration as a possible replacement for organic materials.[16–18] Ahmad *et al.* conducted a simulation of a $Cs_3Bi_2I_9$-based two-dimensional PSC device, utilizing TiO_2 as the ETL and Spiro-MeOTAD as the HTL, with gold serving as the back contact.[19] The simulation indicates that the PSC device attained an η of 11.54%. Researchers are actively engaged in stabilizing experimental PSC devices against various environmental factors, including moisture and temperature. Hamukwaya *et al.*[20] conducted an experiment to examine the performance effects of incorporating KI as an additive in $Cs_3Bi_2I_9$ PL. The incorporation of KI resulted in a peak η of 2.81%. $Cs_3Bi_2I_9$ PL greatly improves the stability of the resulting PSC device against humidity, preserving 98% of the primary PCE after 90 days, thus demonstrating its suitability for SC applications.

Within the same group as lead, tin was considered to be a more favorable alternative for substitution. Tin-based perovskite materials exhibit significant instability due to the relatively low atomic weight of tin, which facilitates the oxidation of Sn^{2+} to Sn^{4+}. Lattice distortion and phase instability might be caused by Sn^{2+} having a much smaller ionic radius compared with Pb^{2+}.[21] The fact that Bi is next to Pb implies that Bi^{3+} is more compatible with Pb^{2+} rather than the other way around. In comparison with perovskites based on Sn, those based on Bi are more stable. Consequently, there has been a surge in the amount of studies examining the photovoltaic capabilities and η of perovskite materials based on Bi.[22–36]

A Bi-based ternary halide perovskite having a chemical formula of $A_3Bi_2I_9$ (A: Cs^+ and MA^+) was reported by Johansson *et al.*[37] Devices using the $Cs_3Bi_2I_9$ film as the AL achieved a PCE of 1.09%. A tiny $A_3Bi_2I_9$ (A = MA^+, Cs^+ or FA^+) film was prepared using a solvent-engineering approach by Buonassisi *et al.*[38] Their devices achieved the maximum PCE of 0.71%.

The study performed by Jain *et al.* demonstrated that BiI_3 films exposed to MAI vapors were able to achieve high stability and increase the PCE of $MA_3Bi_2I_9$ based SCs to 3.17%.[39] The low crystallinity of $MA_3Bi_2I_9$, its wide and indirect band gap, and the presence of non-dense films is responsible for the actual conversion η being much lower than the theoretically anticipated 22.6%. Improving the crystallinity and narrowing the band gap of bismuth-based perovskite films is a top priority.

Combining iodine with bromine or chloride allows halide perovskite materials to have their tuned band gap.[40–48] Currently, the application of band engineering through compositional changes at the anion site in these compounds make them the infrequent PSC. Yu *et al.*[49] characterized $Cs_3Bi_2I_{9-x}Br_x$ perovskite materials through the incorporation of Br into $Cs_3Bi_2I_9$, a type of perovskite made of inorganic bismuth halide, which are more stable. The band gap of 2.03 eV is at its lowest for $Cs_3Bi_2I_6Br_3$ at $x = 3$, whereas $Cs_3Bi_2I_9$ has a band gap of 2.20 eV. The substitution of Br by I typically leads to an increased band gap, attributed to the lower energy of the Br valence p orbital. This phenomenon is notably atypical. The 2D perovskite $Cs_3Bi_2I_6Br_3$ exhibits almost broad ordering of iodine and bromine atoms.[50]

The $Cs_3Bi_2I_6Cl_3$ compound in this family is reported by McCall *et al.*[51] The structure of this compound is a 2D bilayer arrangement of $Cs_3Bi_2Br_9$, with I atoms covering the bilayers and Cl occupying the connecting sites. The absorption edge of this compound remains consistent with that of the 0D parent $Cs_3Bi_2I_9$; however, the notable excitonic peak present in $Cs_3Bi_2I_9$ is not observed in the 2D structure. As the bridging ligand between the octahedral bilayers, Cl does not take part in the band edge states, according to density functional theory (DFT) calculations with the direct band gap of $Cs_3Bi_2I_6Cl_3$. This compound possesses a direct band gap, which is crucial for photovoltaic systems to absorb light and turn it into electricity.

Enhancing the dimensionality of $Cs_3Bi_2I_9$ *via* halide mixing has proven to be a highly efficient method for manipulating the structures and properties of halide compounds due to the significance of structural and electronic dimensions, especially halide perovskites. The band gap of perovskites with compatible structures can be tuned by mixing nearby halides (Br–I or Cl–Br), while mixing dissimilar Cl and I, which has a dramatic impact on optoelectronic properties and can even force the formation of new structures or compounds like in the recently discovered $Cs_2PbI_2Cl_2$.[52–54] It is recently reported that the 2D defect perovskite $Rb_3Bi_2I_6Cl_3$ exhibited essentially perfect ordering of the I and Cl atoms with a band gap value of 2.02 eV.

Considering the impact of mixing of I and Cl as well as the replacement of Rb by Cs ($Rb_3Bi_2I_6Cl_3$ and $Rb_3Bi_2I_3Cl_6$) halide perovskites, DFT calculations were performed in the current study to thoroughly examine the structural features, optoelectronic and photocatalytic properties of these compounds using WIEN2k. Electronic properties indicate their direct band gap semiconductor nature while optical parameters specify that

they are active absorbers for their light-harvesting capacities. The effective mass, higher mobility of electron, exciton binding energy and exciton radius indicate their importance as a solar cell and photo catalyst. Therefore, the SC performance of the compound was determined using SCAPS-1D. To decrease the time and cost associated with the experimental fabrication of numerous SC configurations, numerical analysis were performed to derive a highly efficient SC architecture. A comprehensive investigation of various ETLs and HTLs was performed to identify the optimal combination for the AL ($Rb_3Bi_2I_6Cl_3$ and $Rb_3Bi_2I_3Cl_6$) in which FTO/TiO_2–SnO_2/$Rb_3Bi_2I_6Cl_3$ and $Rb_3Bi_2I_3Cl_6$/MoO_3/Ni combination was recognized as the best configuration. Additionally, the impact of HTL, ETL, thickness of absorber, HTL and ETL, and the effect of defect densities and of back metal contact on SC parameters (*V*oc, *J*sc, FF, and PCE) was evaluated. Several promising and competitive configurations for $Rb_3Bi_2I_6Cl_3$ and $Rb_3Bi_2I_3Cl_6$ based high-efficiency solar cells have been proposed, offering a constructive research avenue for the design and fabrication of cost-effective, high η, and Pb free $Rb_3Bi_2I_6Cl_3$ and $Rb_3Bi_2I_3Cl_6$ based SC.

2. Computational detail

The WIEN2k program[55] uses the full-potential linear augmented plane wave (FP-LAPW) methodology[56] for calculating the structure and optoelectronic properties of $Rb_3Bi_2I_6Cl_3$ and $Rb_3Bi_2I_3Cl_6$ (within the DFT). Some methods have been developed to handle the exchange-correlation, such as the generalized gradient approximation (GGA)[57] and the Tran and Blaha modified Becke–Johnson potential (TB-mBJ)[58] to achieve good results with a very low processing rate. To avoid the charges from escaping, the FP-LAPW method makes a muffin-tin sphere area and an interstitial zone. The harmonic expansion configuration can be found on a muffin-tin sphere with RMT = 10.0/K_{Max}, close to $L_{Max} = 10$. The 13 × 13 × 13 *K*-points in the Brillouin zone are used to measure the optical properties, and the force is reduced to 1 mRy per Bohr with an expected energy of 0.1 mRy between iterations, according to the Kramers–Kronig relation.

The solar cell performance is determined by taking the device (FTO/TiO_2–SnO_2/$Rb_3Bi_2I_6Cl_3$ and $Rb_3Bi_2I_3Cl_6$/MoO_3/Ni) configuration using SCAPS-1D.[59–61] The light source of intensity 1000 W m^{-2}, temperature of 300 K, frequency of 10^{16} Hz and a voltage range of 0–1.50 V are considered in the simulation. The detailed information for each layer is shown in Table 1.[62,63] Table 2 provides an overview of the flaws at the absorber-HTL interface as well as ETL-AL and provides the properties of metal contacts. The distinguishing energy is set at 0.1 eV,[64] with all faces and interfaces assumed to have zero optical reflectance. Additionally, the defect is considered to be single[65] and eqn (1)–(4) are used in SCAPS-1D to calculate efficiency (PCE), FF, V_{OC} and J_{SC}.[66]

$$FF = \frac{V_{MP} \times J_{MP}}{V_{OC} \times I_{SC}} \quad (1)$$

$$PCE = \frac{FF \times V_{OC} \times I_{SC}}{P_{in}} \quad (2)$$

$$V_{OC} \approx \frac{K_B T}{In} In \frac{J_{SC}}{J_0} \quad (3)$$

$$J_{SC} = \frac{I_{SC}}{A} \quad (4)$$

3. Results and discussion

3.1 Structural properties

Perovskites $R_3Bi_2I_6Cl_3$ have a tetragonal structure with space group *P*3*m*1. There are fourteen atoms in the primitive cell as depicted in Fig. 1. The experimental structure data[51] is used to study the structural properties of the $Rb_3Bi_2I_6Cl_3$ compound while $Rb_3Bi_2I_3Cl_6$ is obtained by interchanging the sites of the I and Cl atom. The GGA exchange correlation potential in the DFT scaffold is utilized to optimize the cell structure for the compound to identify their ground state attributes, and its structure is shown in Fig. 1. According to the relevant Birch–Murnaghan equation of state,[67] as illustrated in Fig. 2, the physical properties of these compounds is determined by their ground state energies (E_0). The lattice parameters obtained for $Rb_3Bi_2I_6Cl_3$ and $Rb_3Bi_2I_3Cl_6$ are given in Table 3. From Table 3, the lattice constant for $Rb_3Bi_2I_6Cl_3$ is $a = 8.371$ Å and $c = 10.258$ Å while for $Rb_3Bi_2I_3Cl_6$ it is $a = 8.351$ Å and $c = 10.244$ Å. The

Table 1 Simulation parameters for different layers using $Rb_3Bi_2I_6Cl_3$ and $Rb_3Bi_2I_3Cl_6$ perovskite as the AL

Parameters	FTO[62]	TiO_2–SnO_2 (ref. 63)	$Rb_3Bi_2I_6Cl_3$ ($Rb_3Bi_2I_3Cl_6$) [Calculated]	MoO_3 (ref. 62)
Thickness (nm)	300	150	900	180
E_g (eV)	3.5	3.1	2.06 (1.996)	3.0
χ_e (eV)	4	4	4.80 (5.07)	2.5
ε	9	9	4.17 (4.41)	12.5
N_c (cm^{-3})	2.02×10^{19}	2.0×10^{19}	6.83×10^{18} (1.57×10^{19})	2.2×10^{18}
N_v (cm^{-3})	1.8×10^{19}	1.8×10^{19}	6.11×10^{19} (8.76×10^{19})	1.8×10^{19}
$V_{Th,\ e}$ (cm s^{-1})	10^7	10^7	1×10^8 (1×10^8)	10^7
$V_{Th,\ h}$ (cm s^{-1})	10^7	10^7	8.65×10^7 (7.68×10^7)	10^7
μ_e (cm^2 V s^{-1})	2×10^1	13.84	9.74×10^2 [optimized]	25
M_h (cm^2 V s^{-1})	1×10^{-1}	25	2.1×10^1 [optimized]	100
N_D (cm^{-3})	10^{15}	1.02×10^{19}	0	0
N_A (cm^{-3})	0	0	10^{17} [optimized]	10^{18}
N_T (cm^{-3})	10^{15}	10^{15}	10^{15} [optimized]	10^{15}

Table 2 Simulation parameters of the interface layer

Parameters[62,63]	Absorber	ETL/Absorber	Absorber/HTL
Type of defect	Neutral	Neutral	Neutral
Cross section for electron (cm^2)	1×10^{-15}	1×10^{-15}	1×10^{-15}
Cross section for hole (cm^2)	1×10^{-15}	1×10^{-15}	1×10^{-15}
Energetic distribution	Single	Single	Single
Energy level with respect to E_v (eV)	0.6	0.65	0.65
Characteristic energy (eV)	0.1	0.1	0.1
Total density (cm^{-3})	10^{14}	1×10^{15}	1×10^{15}
Back contact properties			
Metal work function	5.15		
Surface recombination velocity of electron (cm s^{-1})	1×10^{7}		
Surface recombination velocity of electron (cm s^{-1})	1×10^{5}		

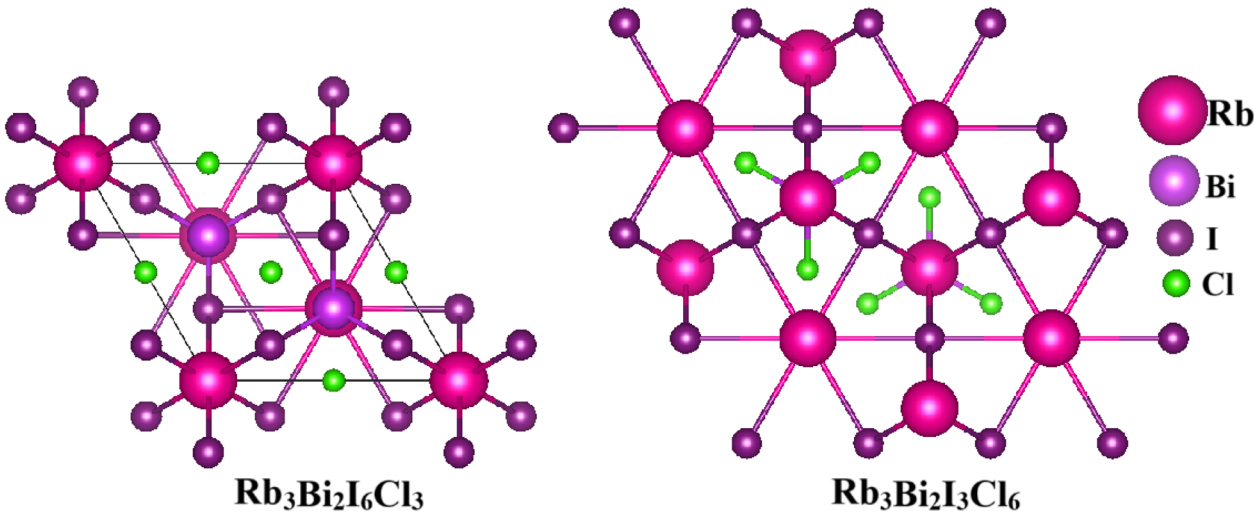

Fig. 1 Crystal structure of $Rb_3Bi_2I_6Cl_3$ and $Rb_3Bi_2I_3Cl_6$ halide perovskites.

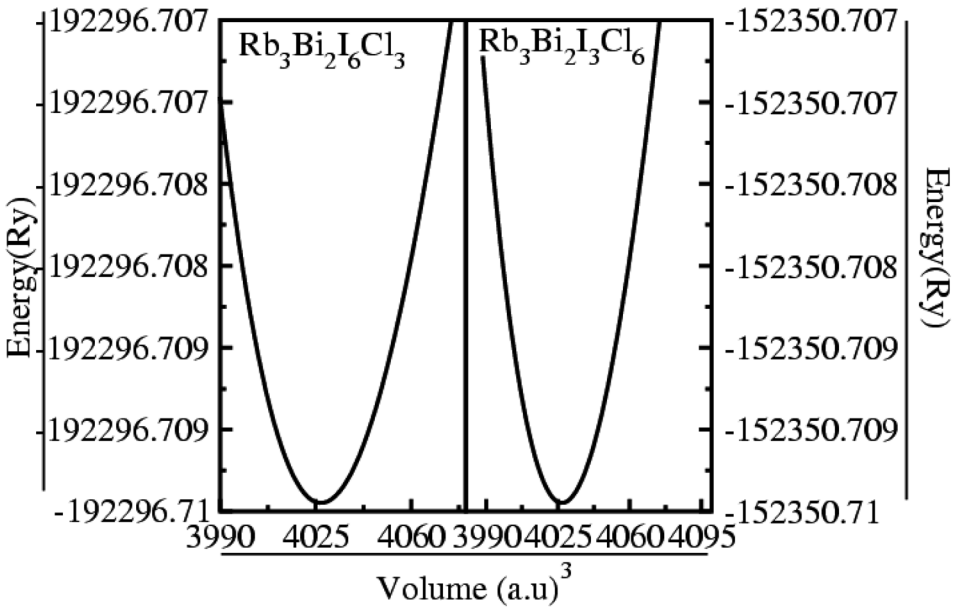

Fig. 2 Energy *versus* volume optimization curve of the $Rb_3Bi_2I_6Cl_3$ and $Rb_3Bi_2I_3Cl_6$ halide perovskites.

Table 3 Calculated lattice constants, bulk modulus, ground state energy, formation enthalpy, band gap, effective masses, exciton energy and exciton Bohr radius of $Rb_3Bi_2I_6Cl_3$ and $Rb_3Bi_2I_3Cl_6$

Parameters	$Rb_3Bi_2I_6Cl_3$	Other[51]	$Rb_3Bi_2I_3Cl_6$
a (Å)	8.3714	8.3673	8.3517
c (Å)	10.2584	10.2506	10.2447
B_0 (GPa)	54.76	—	44.73
E_0 (Ry)	−192296.1194	—	−152350.7131
ΔH (Ry)	−1.7935	—	−0.3269
Band gap E_g (eV)			
TB-mBJ	Γ–M Γ–Γ	Exp.	Γ–M Γ–Γ
	2.051 2.069	2.02	1.996 1.996
m_e^*	0.42 m_e	—	0.73 m_e
m_h^*	1.81 m_e	—	2.30 m_e
E_b^x (meV)	200.63	—	363.68
E_b^z (meV)	225.42	—	305.62
a_x^* (Å)	7.47	—	4.88
a_z^* (Å)	7.05	—	4.76

given results for $Rb_3Bi_2I_3Cl_6$ is fairly close to the experimentally reported lattice constants for $Rb_3Bi_2I_5Cl_4$.[51] The compounds under investigation had a bulk moduli (B_0) of 54.76 and 44.73 GPa, correspondingly which show that $Rb_3Bi_2I_6Cl_3$ is resistant to degradation due to a higher B_0 value compare with $Rb_3Bi_2I_3Cl_6$.

The enthalpy of formation (H_f) is a critical stability parameter that has been derived[68] from E_0 (−192296.1194 Ry and (−152350.7131) and is presented in Table 3. The compound's electrons and nuclei interact through coulombic forces, causing the system to display a greater H_f, suggesting a strong integration and firm connection. As the H_f rises, the system gets increasingly bound because of the contact between electrons and nuclei. The binding strength is independent of the particle size and the number in a given chemical. H_f for $Rb_3Bi_2I_6Cl_3$ is −1.793 Ry and for $Rb_3Bi_2I_3Cl_6$ is −0.326 Ry. The negative value of H_f proves that both compounds are thermodynamically stable while $Rb_3Bi_2I_6Cl_3$ is more stable than $Rb_3Bi_2I_3Cl_6$, which is evidenced from both bulk modulus and enthalpy of formation.

3.2 Electronic properties

There is a correlation between a material's electrical band structure and several physical properties and compounds. Due to the fact that each compound has a distinct band structure, its electrical properties are also distinct.

Fig. 3 shows the determined electronic band structures (EBS) of $Rb_3Bi_2I_6Cl_3$ and $Rb_3Bi_2I_3Cl_6$ compounds. The compounds are direct band gap (E_g) semiconductors, as shown by the EBS, which displays that the gamma symmetry point is shared by the valence band maxima (VB_{max}) and the conduction band minima (CB_{min}). $Rb_3Bi_2I_6Cl_3$ has a direct E_g of 2.061 eV at the Γ point and indirect E_g of 2.051 eV at the Γ–M point, respectively, shown in Table 3. Both direct and indirect E_g of 1.996 eV have been determined for $Rb_3Bi_2I_3Cl_6$ at Γ and Γ–M points. The E_g of 2.02 eV was reported experimentally for $Rs_3Bi_2I_6Cl_3$ using the absorption edge method.[51]

The density of states (DOS), which shows how many states a system can have at a given energy level, determines the bulk material's properties. Fig. 4 shows the calculated total DOS (TDOS) of the compounds under study, with the Fermi level (EF)

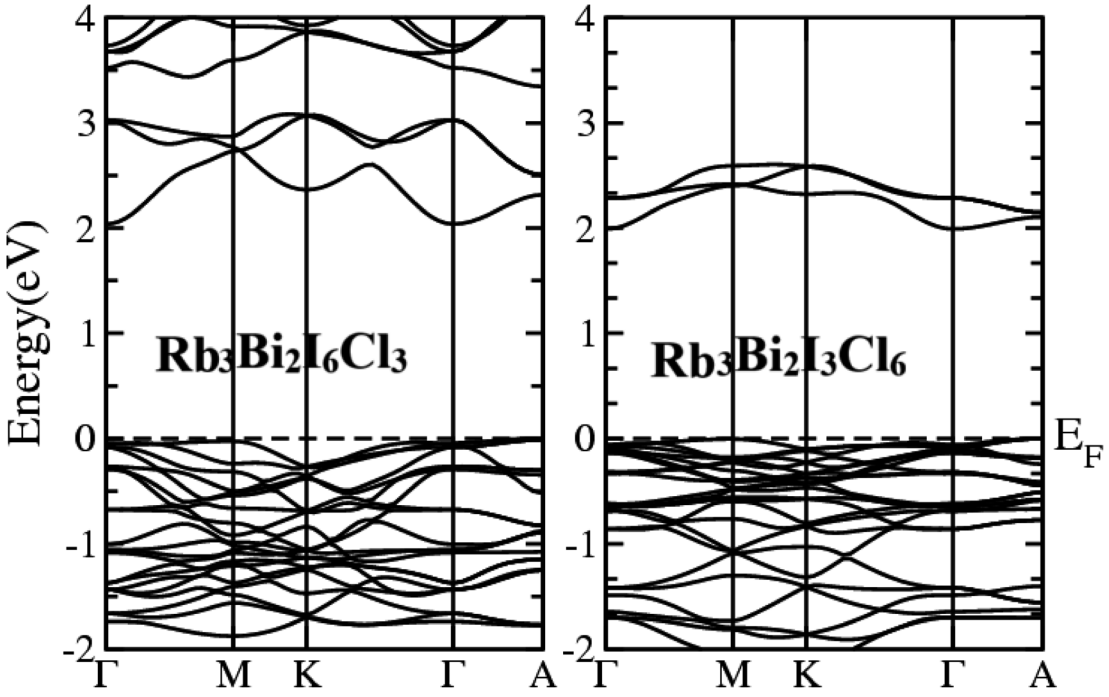

Fig. 3 Electronic band structure of the $Rb_3Bi_2I_6Cl_3$ and $Rb_3Bi_2I_3Cl_6$ halide perovskites.

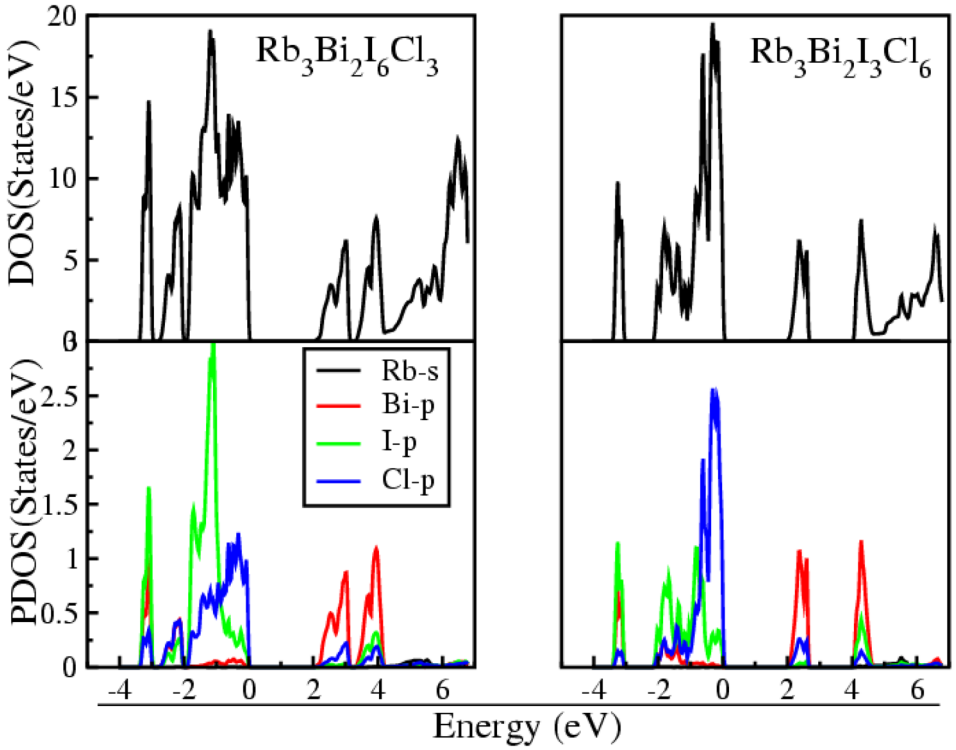

Fig. 4 Total DOSs and partial DOSs of the $Rb_3Bi_2I_6Cl_3$ and $Rb_3Bi_2I_3Cl_6$ halide perovskites.

fixed at 0 eV. There is no energy gap flanked by VB and CB, and the fact that E_F does not cross densities indicates that both compounds are semiconductors, according to the TDOS. The precise E_g for the compound in the present study was determined and compared with the other reported DFT result.[51] The analysis verifies that TB-mBJ calculations and experimental E_g

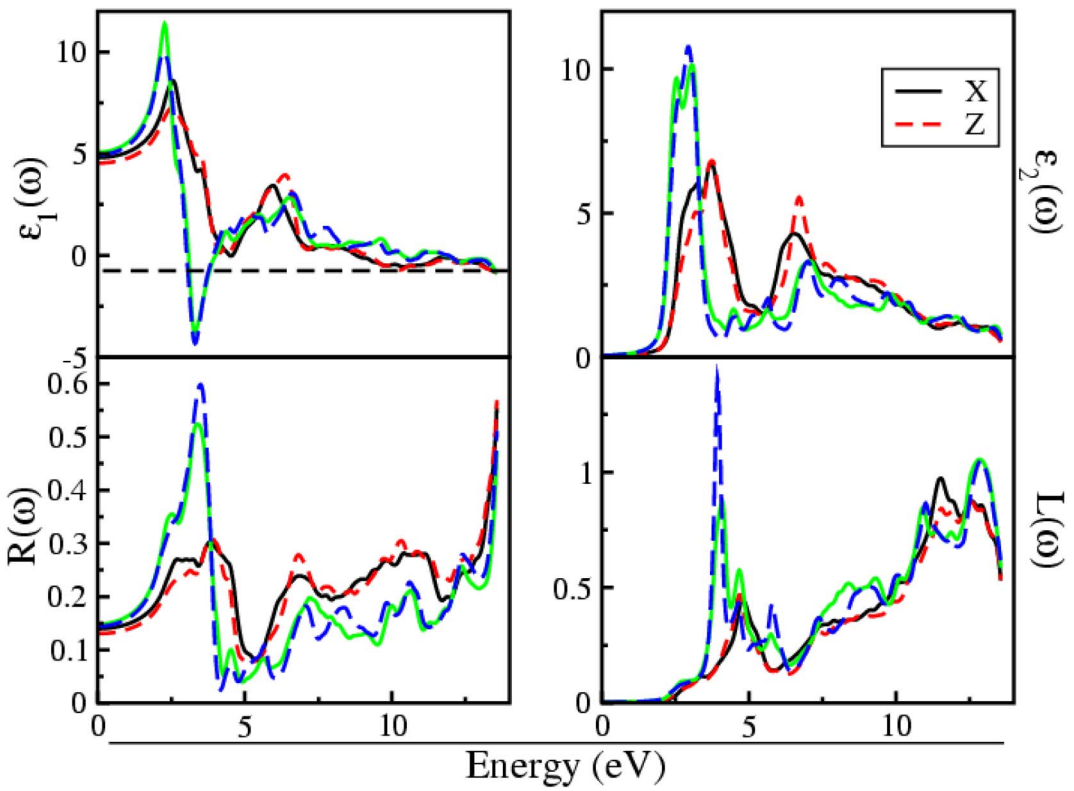

Fig. 5 Dielectric function, reflectivity and loss function of the $Rb_3Bi_2I_6Cl_3$ and $Rb_3Bi_2I_3Cl_6$ halide perovskites.

are credible[51] and the findings of the E_g for these compounds using TB-mBJ are reliable and supported by solid scientific evidence.[69–71]

The PDOS of these compounds has been computed and is shown in Fig. 4, providing appreciated understandings into their semiconducting properties. Fig. 4 illustrates the involvement of various atomic states, such as the Rb-s, Bi, I and Cl p states. Notably, the influence of the Rb-s state is minimal, while the p state of Bi, I and Cl have a substantial role. In the VB, the I and Cl-p state influence within a range of −3.8–zero eV, while in the conduction band Bi-p state, it spans from the E_g to 4.8 eV, with distinct differences in contributions between the VB and CB. In the compounds, the Bi, I and Cl-p states have a greater impact on the VB and CB, and the energy difference between the VB and CB is caused by the Bi-p and Cl-p states.

3.3 Optical properties

Studying the optoelectronic performance of these compounds requires an understanding of the behavior of light waves. The optical properties of these $Rb_3Bi_2I_6Cl_3$ and $Rb_3Bi_2I_3Cl_6$ compounds is explored by taking energy from 0 to 14 eV and are shown in Fig. 5 and 6.

The dielectric function, as shown in Fig. 5, provides insight into the compound's physical characteristics ($\varepsilon_1(\omega)$). The static dielectric function, also known as $\varepsilon_1(0)$ at zero eV are 4.80, 4.53, 5.07 and 4.94 eV at x and z axis respectively for $Rb_3Bi_2I_6Cl_3$ and $Rb_3Bi_2I_3Cl_6$ presented in Fig. 4. For both compound spectra shown after zero frequency show peaks at 8.60, 5.01, 11. 37 and 9.95 eV respectively at x and z axis. Once the spectra level out after this peak, they start to behave more like metal and less like dielectrics at energy values close to zero.

Fig. 5 shows the $\varepsilon_2(\omega)$ values, demonstrating no spectra within the optical gap, which are 2.051 and 2.054 eV at the x and z axis, respectively for $Rb_3Bi_2I_6Cl_3$ and 2.0 eV at both the x and z axis for $Rb_3Bi_2I_3Cl_6$. The optical gap is active in visible light, making it appropriate for solar cell applications. In Fig. 5, the spectra display a steep ascent in the curve following the threshold value, with interband transition peaks at 6.70, 6.81 9.67 and 10.76 eV at x and z axis.

The ($R(\omega)$) and the reflectance at zero energy ($R(0)$) at the x and z axes for $Rb_3Bi_2I_6Cl_3$ are 13.0% and 13.4%, respectively, while for $Rb_3Bi_2I_6Cl_3$, they are 14.8% and 14.4%, respectively (Fig. 5). $Rb_3Bi_2I_6Cl_3$ exhibits a greater reflectivity of 29.7% and 30.8% at 3.49 eV while $Rb_3Bi_2I_3Cl_6$ exhibits higher reflectivity of 52.8% and 59.8% at 4.87 eV respectively. When the energy reaches the point where $\varepsilon_1(\omega)$ becomes zero, the $R(\omega)$ starts to increase. These compounds demonstrate a high reflectance in the ultraviolet (UV) spectrum, suggesting their potential as a guard beside high-frequency radiation.

Fig. 4 displays the $L(\omega)$, representing the electrons passing through a material. This value relies on the momentum and loss of energy.[72] These compounds exhibit a peak in their curves due to resonance with the plasma frequency. When the photon energy exceeds the E_g value, scattering is absent, revealed by Fig. 5. The maximum $L(\omega)$ for these compounds can be observed in Fig. 5, ranging from 3.5 to 5 eV and from 10.5 to 12.20 eV. This variation is attributed to discrete energy bands.

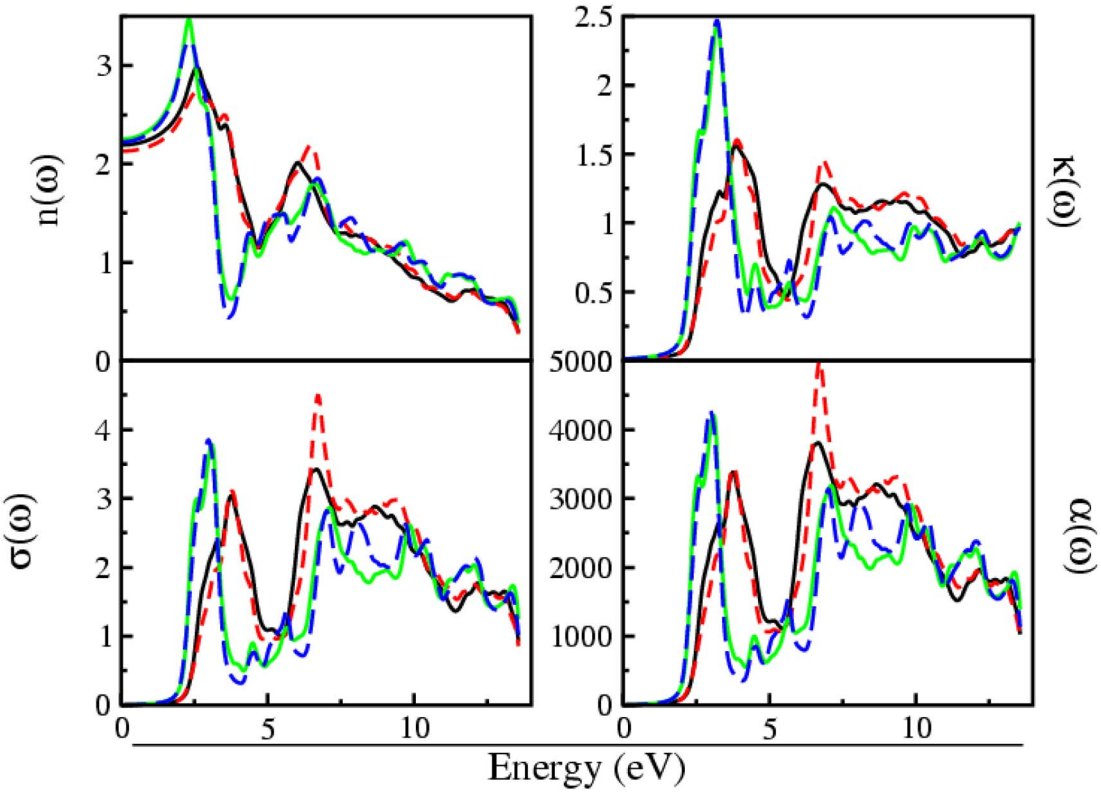

Fig. 6 Refractive index, oscillator strength, excitation coefficient and optical conductivity of the $Rb_3Bi_2I_6Cl_3$ and $Rb_3Bi_2I_3Cl_6$ halide perovskites.

The $n(\omega)$ values characterize the refractive index for the compound being studied in Fig. 6. For the $Rb_3Bi_2I_6Cl_3$ compound, the $n(\omega)$ value at 0 eV is represented by ($n(0)$) and is 2.19 and 2.12 at x and z axes, while the $n(0)$ for $Rb_3Bi_2I_3Cl_6$ occurs at 2.25 and 2.22 at the x and z axes, respectively. The $n(\omega)$ begins to increase and reach to its peak value, representing that the highest energy value of $n(\omega)$ are 2.57, 2.59 eV and 2.29, 2.35 eV. The compounds being studied exhibit significant $n(\omega)$ values, resulting from the limited transmission of light rays *via* the materials.[73]

The light matter interaction is expressed by the extinction coefficient, which is abbreviated as $k(\omega)$.[74] We can reasonably expect a material with a modest $k(\omega)$ to have high transmittance and low absorption. These compounds' $k(\omega)$ has a strong relationship with $\varepsilon_2(\omega)$.

The fact that the $k(\omega)$ values are mostly 0 up to the E_g, as seen in Fig. 6, suggests that there is negligible absorption and strong transmission. The results show that these compounds have poor transmission and high light absorption at these energy levels, with the maximum values of 1.56 at 3.85 eV and 1.60 at 3.87 eV as well as 2.45 at 3.22 and 2.46 at 3.22 eV.

How well a material lets electrons pass through it when an electromagnetic field is applied is defined by its $\sigma(\omega)$. Fig. 6 shows the spectra of the $Rb_3Bi_2I_6Cl_3$ and $Rb_3Bi_2I_3Cl_6$ compounds which indicate that optical conduction begins at the band gap value and continues to rise beyond it, reaching its peak conductivity for these compounds. These compounds demonstrate a maximum $\sigma(\omega)$ of 3.42, 4.48 and 3.77, 3.84 Ω^{-1} cm^{-1} at 6.37 and 2.97 eV, as illustrated in Fig. 6.

The $\alpha(\omega)$ value is an important parameter for calculating the absorption of light per unit length of light. Optical absorption occurs when the incoming photon frequency resonates with the transition frequency of the atom. For the transition of electrons from VB to CB, the energy of the incoming photon should be greater than the E_g energy. Fig. 6 indicates that absorption starts at an energy greater than the E_g energy that is around 2 eV. After that, the curve increases and achieves maximum absorption peaks of 3807.68, 4995.13, 4205.62, and 4280.22 cm^{-1} at 6.68, 6.70 and 3.08, 2.97 eV, respectively. This indicates that these materials can be used as a shield in the ultraviolet region and as a solar cell in the visible region.

To analyze the energy levels in solar devices and photocatalytic applications in depth, the effective mass calculation is crucial. Electron and hole conductivity effective masses influence free-carrier optical response, electrical resistivity, mobility, and photovoltaic applications.[75] The effective masses of the electron and the hole were determined by post-processing band structures to get insight into the materials' electron/hole conduction characteristics. The effective mass for the electron and holes are 0.42 m_e and 1.81 m_e for $Rb_3Bi_2I_6Cl_3$ and 0.73 m_e and 2.30 m_e for $Rb_3Bi_2I_3Cl_6$, as shown in Table 3. Since the effective masses of electrons are smaller than those of the holes, this suggests that the electrons are more mobile than the holes in these compounds.[76] The higher mobility and effective masses of the charge carriers are critical features of photocatalysis that can affect the efficiency of semiconductors. Owing to its high mobility, which is inversely proportional to effective mass, these compounds are interesting candidates for applications involving photocatalysis and efficient photoconduction.

Furthermore, the exciton characteristics are examined for these compounds by determining the exciton radius (a^*) and exciton binding energy (E_b).[76] The calculated E_b for these compounds are 200.63, 225.42 and 363.68, 305.62 meV at the x and z axis, respectively. The corresponding a^* is 7.47, 70.5 and 4.88, 4.76 Å at the x and z axis for $Rb_3Bi_2I_6Cl_3$ and $Rb_3Bi_2I_3Cl_6$ compounds presented in Table 3. It is evident from Table 3 that the corresponding a^* decreases as the E_b increases. The photogenerated electron and hole charge carriers interact less and dissociate faster due to the bigger exciton radius and lower exciton binding energy, both of which are beneficial for SC applications. The understudy compounds display great promise as materials for SC and photocatalytic application due to their impressive E_g, $\sigma(\omega)$ higher mobility of electron, lower effective mass, less axciton energy and greater axciton radius.

3.4 Simulation and modelling of solar cells

Simulation can greatly enhance the understanding of the physical explanations, physical modifications of device performance such as SCs. Due to the ease of use, capability to simulate in various lighting conditions, and capability to model and build complex heterojunctions without additional measurements, SCAPS-1D is proven to be superior to other competing programs.[77] The optical performance of the compound is analyzed by evaluating its performance in terms of the SC capacitance simulator which determine the η and current density of SC in relation to voltage.[77]

In the current study of the fabricated structures, the layers are arranged in the following order: Li-doped titanium oxide (Li–TiO_2), Al-doped zinc oxide (Al–ZnO), titanium oxide-tin oxide (TiO_2–SnO_2) as ETL, $Rb_3Bi_2I_6Cl_3$ and $Rb_3Bi_2I_3Cl_6$ as the AL, CFTS (Cu_2FeSnS_4), copper oxide (CuO_2), copper iodide (CuI), copper(I) thiocyanate (CuSCN), molybdenum trioxide (MoO_3), nickel oxide (NiO), regioregular poly (3-hexylthiophene-2,5-diyl) (P3HT), poly(3,4-ethylenedioxythiophene) polystyrene sulfonate (PEDOT:PSS) and reduced graphene oxide (rGO) as the HTL and Ni as the back contact, and the corresponding device model is presented in Fig. 7.

The performance of the proposed cell is enhanced primarily through the modification of ETL and HTL in $Rb_3Bi_2I_6Cl_3$ and $Rb_3Bi_2I_3Cl_6$-based PSCs, as depicted in Fig. 8. Fifty six devices were fabricated, and their photovoltaic performances were recorded, as presented in Tables 4–6. Tables 4–6 presents the parameters of photovoltaic systems, including J_{SC}, V_{OC}, FF and PCE. Table 4 presents a higher PCE of 10.68%, accompanied by J_{SC} values of 13.77 mA cm^{-2}, V_{OC} of 1.32 V and FF of 58.53 achieved using NiO as the HTL, Li–TiO_2 as the ETL and $Rb_3Bi_2I_6Cl_3$ as the AL, while all other devices exhibited lower photovoltaic parameters. Using CuSCN and MoO_3 as the HTL results in the highest photovoltaic performance, achieving a PCE of 10.74%. This is characterized by a J_{SC} of 9.22 and 8.86 mA cm^{-2}, a V_{OC} of 1.15 and 1.41 V, and a fill factor (FF) of 72.90 and 82.93 with Li–TiO_2 as the ETL and $Rb_3Bi_2I_3Cl_6$ as the AL compared with other examined HTLs as shown in Table 4.

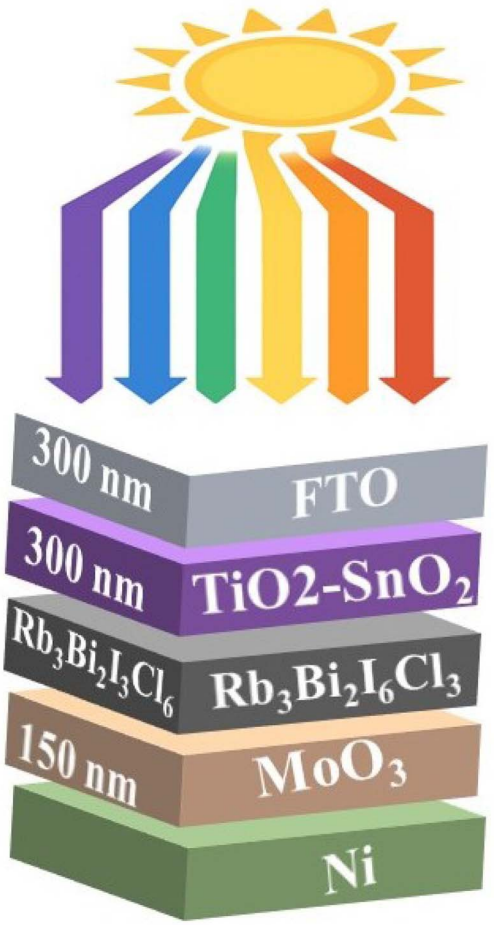

Fig. 7 Schematic of the solar cell device having $Rb_3Bi_2I_6Cl_3$ and $Rb_3Bi_2I_3Cl_6$ as an absorber layer.

In a similar manner, Al–ZnO taken as the ETL demonstrates optimal performance, achieving a PCE of 10.87 and 11.64%, with a J_{SC} of 9.12 and 10.21 mA cm^{-2}, an V_{OC} of 1.41 and 1.35 V, and an FF of 84.12 and 84.01 when paired with MoO_3 as a HTL for both compounds used as AL as shown in Table 5.

Additionally, when hybrid ETL TiO_2–SnO_2 is used with MoO_3 as the HTL, it achieves a PCE of 10.83 and 11.52%, with a J_{SC} of 9.02 and 10.11 mA cm^{-2}, an V_{OC} of 1.41 and 1.35 V, and an FF of 84.69 and 83.93 as indicated in Table 6 compared with all other HTL for both compounds as an absorber layer.

In summary, MoO_3 demonstrates optimal performance as an HTL with Al–ZnO as the ETL among various HTLs. This is attributed to its excellent conductivity, which improves charge collection mechanisms, and its favorable band alignment, which protects the device performance from interfacial trap effects. Although Al–ZnO has not been widely utilized as an ETL material in existing literature, it has recently garnered attention for this application in PSC owing to its favorable stability, cost-effectiveness, compatibility with various perovskites and high electron mobility. The PCE of the $Rb_3Bi_2I_6Cl_3$ and $Rb_3Bi_2I_3Cl_6$ based devices show that the $Rb_3Bi_2I_3Cl_6$ based device has improved PV performance compared with the $Rb_3Bi_2I_6Cl_3$ based device; therefore, using $Rb_3Bi_2I_3Cl_6$ perovskite as an absorber in

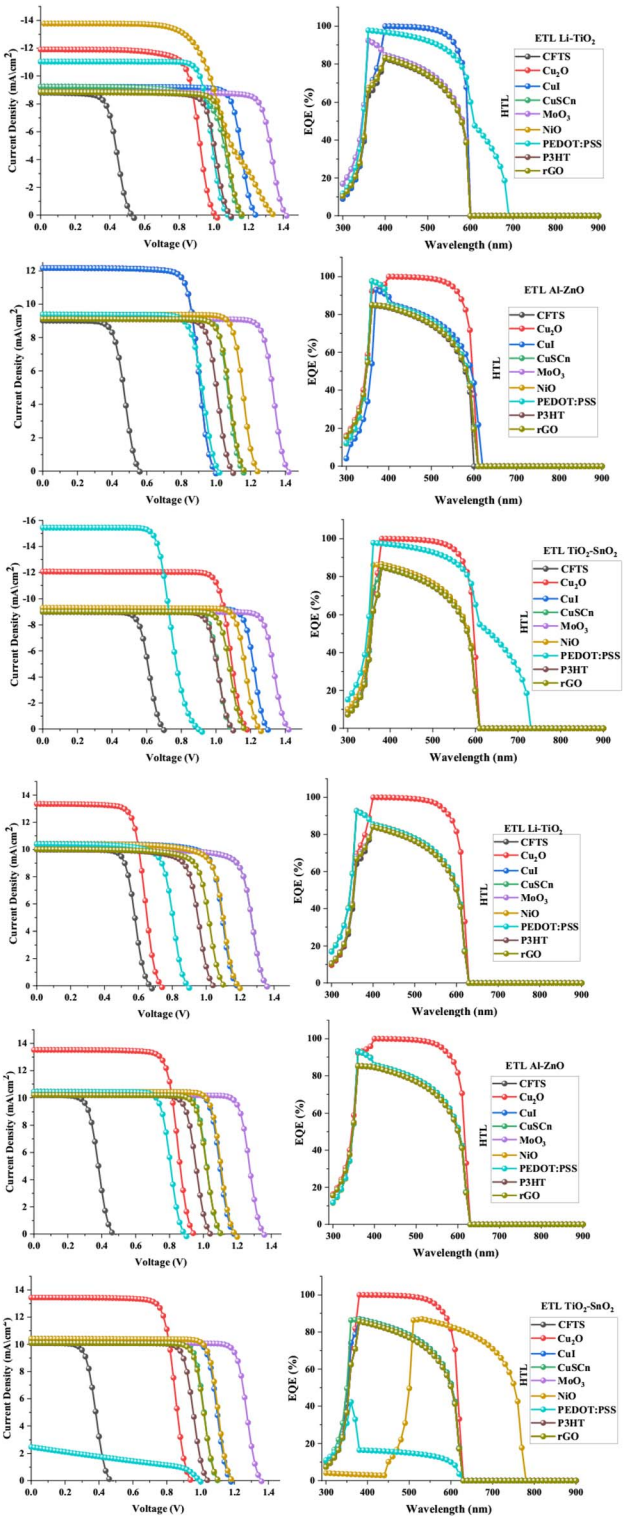

Fig. 8 *J versus V* characteristic and quantum efficiency against photon energy of the solar cell device using $Rb_3Bi_2I_6Cl_3$ and $Rb_3Bi_2I_3Cl_6$ as an absorber layers.

solar cells shows exciting prospects due to the higher PCE of the $Rb_3Bi_2I_3Cl_6$ absorber compared with the $Rb_3Bi_2I_6Cl_3$ absorber.

The ratio of captured electron–hole pairs to striking photons determines the quantum η of a SC, which can be expressed in

Table 4 *J–V* characteristic of absorber with different HTLs and Li–TiO_2 as the ETL

HTL	ETL	V_{OC} (v)	J_C (mA cm^{-2})	FF (%)	PCE (%)
CFTS	Li–TiO_2	0.52 (0.66)	8.81 (9.98)	64.74 (71.27)	3.0 (4.74)
Cu_2O		1.00 (0.73)	11.89 (13.35)	74.62 (70.91)	8.94 (6.91)
CuI		1.24 (1.18)	9.22 (10.40)	82.00 (77.99)	9.39 (9.59)
CuSCN		1.15 (1.53)	9.22 (10.03)	72.90 (78.89)	7.77 (10.74)
MoO_3		1.41 (1.36)	8.86 (10.03)	82.93 (78.89)	10.42 (10.74)
NiO		1.32 (1.18)	13.77 (10.40)	58.53 (76.46)	10.68 (9.44)
PEDOT: PSS		1.08 (0.88)	11.02 (10.14)	79.24 (73.36)	9.45 (6.78)
P3HT		1.09 (1.04)	8.85 (10.01)	79.40 (74.98)	7.69 (7.82)
rGO		1.16 (1.10)	8.85 (10.02)	80.31 (75.91)	8.28 (8.40)

Table 5 J-V characteristics of the absorber with different HTLs and Al–ZnO as the ETL

HTL	ETL	V_{OC} (v)	J_C (mA cm^{-2})	FF (%)	PCE (%)
CFTS	Al–ZnO	0.55 (0.46)	9.01 (10.86)	66.00 (61.68)	3.32 (2.92)
Cu_2O		0.99 (0.94)	12.16 (13.52)	77.05 (76.05)	9.30 (9.70)
CuI		1.24 (1.18)	9.35 (10.44)	82.62 (82.12)	9.58 (10.13)
CuSCN		1.15 (1.10)	9.38 (10.44)	81.51 (81.09)	8.83 (9.34)
MoO_3		1.41 (1.35)	9.12 (10.21)	84.12 (84.01)	10.87 (11.64)
NiO		1.23 (1.18)	9.38 (10.44)	82.89 (82.21)	9.61 (10.19)
PEDOT:PSS		1.01 (0.88)	9.37 (10.44)	77.05 (77.79)	7.33 (7.22)
P3HT		1.01 (1.04)	9.17 (10.20)	80.47 (79.85)	8.02 (8.48)
rGO		1.16 (1.10)	9.12 (10.20)	85.37 (80.80)	8.83 (9.10)

Table 6 *J–V* characteristics of the absorber with different HTLs and TiO_2–SnO_2 as the ETL[a]

HTL	ETL	V_{OC} (v)	J_C (mA cm^{-2})	FF (%)	PCE (%)
CFTS	TiO_2–SnO_2	0.69 (0.46)	8.99 (10.07)	72.81 (62.09)	4.55 (2.91)
Cu_2O		1.17 (0.94)	12.07 (13.43)	80.18 (76.07)	10.83 (9.64)
CuI		1.29 (1.17)	9.24 (10.35)	84.20 (82.67)	10.09 (10.06)
CuSCN		1.08 (1.10)	9.23 (10.40)	81.83 (81.38)	8.22 (9.33)
MoO_3		1.41 (1.35)	9.02 (10.11)	84.69 (83.93)	11.39 (11.52)
NiO		1.24 (1.18)	9.31 (10.41)	83.41 (82.47)	9.70 (10.17)
PEDOT: PSS		0.89 (0.99)	15.44 (2.47)	68.50 (37.05)	9.49 (0.91)
P3HT		1.09 (1.04)	9.01 (10.10)	81.14 (80.07)	7.91 (8.42)
rGO		1.16 (1.10)	9.09 (10.10)	82.05 (81.00)	8.61 (9.04)

[a] ETL.

terms of wavelength (nm).[78] Fig. 8 displays the measurements of quantum efficiency (QE) against the wavelength range from 300 to 900 nm. The use of $Rb_3Bi_2I_6Cl_3$ and $Rb_3Bi_2I_3Cl_6$ as absorbers shows maximum QE of 16.94 and 17.15%, respectively at 300 nm with Li–TiO_2 as the ETL while MoO_3 and NiO are the HTL and reaches a maximum value of 99% between 400 and 490 nm, which gradually decreases to 67.70% at 590 nm for Cu_2O and CuI as the HTL with $Rb_3Bi_2I_6Cl_3$ as an absorber while Cu_2O as the HTL shows these maximum values for the $Rb_3Bi_2I_3Cl_6$ absorber. Similarly, when AL-ZnO is taken as the ETL, the $Rb_3Bi_2I_6Cl_3$ and $Rb_3Bi_2I_3Cl_6$ absorbers show QE of 15.61 and 15.64%, respectively at 300 nm with MoO_3 as the HTL and shows a maximum value of 99% between 380 and 490 nm and gradually decreases to 37.51% at 600 nm and 33.03% at 620 nm using Cu_2O as the HTL. Likewise, when TiO_2–SnO_2 is taken as the ETL, the QE for the PEDOT:PSS HTL is 15.21% and 11.05% using the absorbers $Rb_3Bi_2I_6Cl_3$ and $Rb_3Bi_2I_3Cl_6$, respectively, at 300 nm and shows a maximum value of 99% between 380 and 490 nm and gradually decreases to 37.51% at 600 nm and 33.03% at 620 nm for the HTL Cu_2O.

When it comes to the visible spectrums, the device is capable of efficiently converting photon energy into electricity. However, the QE starts to decline as the wavelengths get longer and the energy decreases.

Through the Cu_2O HTL, NiO and PEDOT: PSS shows the maximum QE while both the absorbers shows maximum PCE for the MoO_3 HTL due to the issues with carrier transport and recombination at the interfaces and a low FF can significantly reduce PCE even with a high EQE and a low *V*oc can lead to a lower PCE.[62,63]

The PCE of the FTO/TiO_2–SnS_2/$Rb_3Bi_2I_6Cl_3$ and $Rb_3Bi_2I_3Cl_6$/MoO_3/Ni devices was compared with the other Bi based

Table 7 PCE comparison with other double and triple perovskite base absorbers for solar cells

Absorber	PCE (%)	Method	Ref.
$MA_3Bi_2I_9$	0.08	Spin coating	22
$MA_3Bi_2I_9$	0.42	Spin coating	23
$MA_3Bi_2I_9$	0.39	Evaporation spin coating	24
$MA_3Bi_2I_9$	0.36	Solvent engineering spin coating	25
$MA_3Bi_2I_9$	0.31	Spin coating	26
$MA_3Bi_2I_9$	0.26	Spin coating	27
$MA_3Bi_2I_9$	0.19	Spin coating	28
$MA_3Bi_2I_9$	0.12	Spin coating	29
$MA_3Bi_2I_9$	0.08	Spin coating	30
$(MA_3Bi_2I_9)_{0.2}(BiI_3)_{0.8}$	1.09	Spin coating	29
$Cs_3Bi_2I_9$	0.21	Spin coating	31
$Cs_3Bi_2I_9$	3.20	Spin coating	32
$Cs_3Bi_2I_9$	0.40	Spin coating	33
$Cs_3Bi_2I_9$	11.14	Simulation	34
$CsBi_3I_{10}$	1.51	Spin coating	36
$CsBi_3I_{10}$	1.51	Spin coating	36

perovskites as an absorber for SC and was presented in Table 7. The PCE of isotropic perovskites as an absorber range from 0.08 to 11.14% respectively. The improved PCE of the perovskite under study as an absorber in the current work highlights the importance of this research focused on environmentally friendly Pb-free perovskite solar cells.

3.5 Photocatalytic properties

Special optical and electrical characteristics of a material is necessary for photocatalytic processes. An ideal crystal for photocatalytic water splitting would have the following critical properties: an appropriate band gap, band edge levels, optical absorbance, and effective carrier masses. Most significantly, each of these perovskites has a suitable band gap between 1.5 and 3.0 eV in the visible light spectrum. To ascertain the photocatalytic water splitting potential, the Mulliken electronegativity technique was used to examine the photocatalytic characteristics of these 2D perovskites. The ECB and EVB are estimated using the relations respectively. The χ value is the geometric mean of the electronegativity,[79] a crucial component in determining a material's electrical characteristics and the electron's free energy.

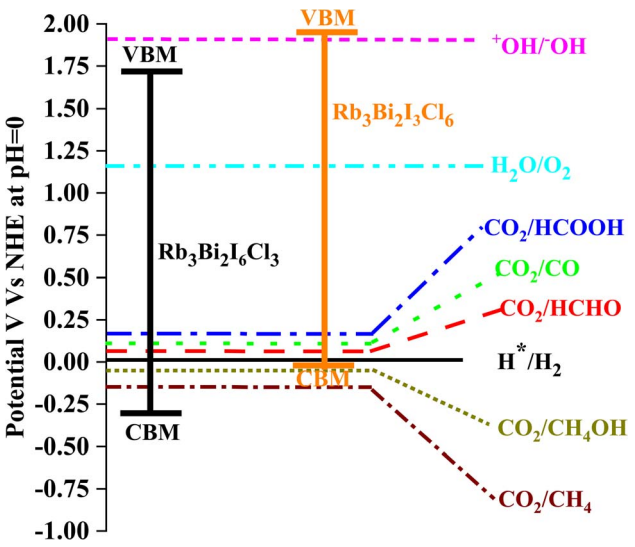

Fig. 9 Band edges of $Rb_3Bi_2I_6Cl_3$ and $Rb_3Bi_2I_3Cl_6$ halide perovskite compared with the redox potentials of the water-splitting reaction and CO_2 reduction photodegradation processes in a normal hydrogen electrode (NHE) at pH 0.

The semiconductor material used for effective photocatalytic water splitting should satisfy two requirements: (1) the valence band maximum should be more positive than the potential edge of H_2O/O_2, and (2) the semiconductor's conduction band minimum should be more negative than the redox potential of H^*/H_2 (0 V *vs.* NHE).[80] These standards are applicable to the photocatalytic process of CO_2 reduction. It was observed that the materials' EVB values were higher than 1.23 V (the potential of O_2) and their ECB values were less than 0 V (the redox potential of H_2). For photo-catalytic water splitting, these 2D perovskites are appropriate for water splitting driven by visible light, as shown in Fig. 9. It was also demonstrated that the EVB of $Rb_3Bi_2I_6Cl_3$ perovskite was more negative for the CO_2 reduction process than CO_2/HCOOH, CO_2/CO, CO_2/HCHO, CO_2/CH_4OH and CO_2/CH_4, while $Rb_3Bi_2I_3Cl_6$ perovskite was more negative for the CO_2 reduction process than CO_2/HCOOH, CO_2/CO and CO_2/HCHO and can easily photo-reduce CO_2.[81]

In comparison with other Bi-based compounds, these compounds possess greater positive VBM than the *n*-Bi_2S_3, *n*-Bi_2O_3, *n*-Bi_5O_7I, *n*-$CuBi_2O_4$, *n*-$Bi_2Sn_2O_7$, *n*-$Bi_2Fe_4O_9$, *n*-$Bi_4Ti_3O_{12}$, *n*-$Bi_3Ti_2O_7$ and In–$Bi_4Ti_3O_{12}$; therefore, the compounds under study are more reliable then these compounds in oxygen evaluation reactions. Similarly, these compounds possess greater negative CBM than *n*-Bi_2O_3, *n*-Bi_4O_7, *n*-BiOBr, *n*-BiOI, *n*-$Bi_4O_5Br_2$, *n*-Bi_2MoO_6, *n*-Bi_2WO_6, *n*-$BiVO_4$, *n*-Bi_5O_7I, *n*-$BiFeO_3$, *n*-$Bi_2O_2CO_3$ and $Ca_3Bi_2Br_9$; therefore, the compounds under study are more reliable then these compounds in hydrogen evaluation reactions.[82]

4. Conclusions

This study explored the optoelectronic and structural characteristics of 2D halide $Rb_3Bi_2I_6Cl_3$ and $Rb_3Bi_2I_3Cl_6$ perovskite in the *P*3*m*1 phase through the application of the FPLAPW method in the DFT domain with GGA and TB-mBJ potentials. The experimental values are in perfect agreement with structural parameters estimated by WIEN2k. Compounds $Rb_3Bi_2I_6Cl_3$ and $Rb_3Bi_2I_3Cl_6$ are clearly direct band gap semiconductors (2.02 and 1.99 eV) as shown by band structure TDOS and PDOS calculations. The compounds under study show optical dynamics in the visible part of the electromagnetic spectrum which make them ideal for optoelectronic devices driven by visible light photocatalysis and SC applications. The efficiency of FTO/TiO_2–SnO_2/$Rb_3Bi_2I_6Cl_3$ and $Rb_3Bi_2I_3Cl_6$/MoO_3/Ni based solar cell devices achieved J_{sc} of 9.02 and 10.11 mA cm^{-2}, V_{oc} values of 1.41 and 1.35 V, FF of 84.69 and 83.93 and PCE of 11.39 and 11.52%, respectively. Additionally, the photocatalytic analysis demonstrates that all of the may evolve H_2O/O_2 to O_2 and H^+ to H_2. Additionally the compound under study is also

capable of CO_2 reduction to produce HCOOH, CO, HCHO, CH_4OH and CH_4. Based on these findings, 2D perovskites could be used for optoelectronic, photovoltaic, and photocatalytic devices, especially for water splitting and CO_2 reduction driven by visible light. The findings facilitate future studies aimed at developing fully inorganic perovskite photovoltaics and photocatalysts lacking lead halide, demonstrating improved photovoltaic photocatalytic performance.

Data availability

The data used in the current study are available from the corresponding author upon reasonable request.

Author contributions

Research techniques and writing (reviewing and editing) was performed by Shahid Mehmood. Research data collection, methodology and writing (first draft) was carried out by Shah Rukh Khan. Zahid Ali managed the projects, oversaw the teams, conceptualized the study, and provided expertise in data analysis. Data visualization, formal analysis, editing and review was conducted by Meznah M. Alanazi and Shaimaa A. M. Abdelmohsen. Acquisition of funds, resources, and software was undertaken by Mohmed Mousa.

Conflicts of interest

The authors stated that they have no competing interest.

Acknowledgements

The authors express their gratitude to Princess Nourah bint Abdulrahman University Researchers Supporting Project number (PNURSP2025R132), Princess Nourah bint Abdulrahman University, Riyadh, Saudi Arabia. Access to information and resources Upon reasonable request, the data utilised in this study can be obtained from the correspoinding author.

References

1 A. Fichera, S. Samanta, P. S. Datta, A. Das, M. Sanowar Hossain, A. M. Abdul Mannan, *et al.*, A Comprehensive Review on Recent Advancements in Absorption-Based Post Combustion Carbon Capture Technologies to Obtain a Sustainable Energy Sector with Clean Environment, *Sustainability*, 2023, **15**, 5827, DOI: 10.3390/SU15075827.

2 W. Azam, I. Khan and S. A. Ali, Alternative energy and natural resources in determining environmental sustainability: a look at the role of government final consumption expenditures in France, *Environ. Sci. Pollut. Res.*, 2022, **1**, 1–17, DOI: 10.1007/S11356-022-22334-Z/TABLES/6.

3 D. A. Tofu, K. Wolka and T. Woldeamanuel, The impact of alternative energy technology investment on environment and food security in northern Ethiopia, *Sci. Rep.*, 2022, **12**(12), 1–11, DOI: 10.1038/s41598-022-14521-2.

4 A. Das and S. D. Peu, A Comprehensive Review on Recent Advancements in Thermochemical Processes for Clean Hydrogen Production to Decarbonize the Energy Sector, *Sustainability*, 2022, **14**, 11206, DOI: 10.3390/SU141811206.

5 A. Das, S. D. Peu, MdS. Hossain, M. A. M. Akanda, M. M. Salah, M. M. H. Akanda, *et al.*, Metal Oxide Nanosheet: Synthesis Approaches and Applications in Energy Storage Devices (Batteries, Fuel Cells, and Supercapacitors), *Nanomaterials*, 2023, **13**, 1066, DOI: 10.3390/NANO13061066.

6 E. Zafeiriou, N. Sariannidis, S. Tsiantikoudis, A. Das, S. Datta Peu, A. M. Abdul Mannan, *et al.*, Peer-to Peer Energy Trading Pricing Mechanisms: Towards a Comprehensive Analysis of Energy and Network Service Pricing (NSP) Mechanisms to Get Sustainable Enviro-Economical Energy Sector, *Energies*, 2023, **16**, 2198, DOI: 10.3390/EN16052198.

7 S. Ma, G. Yuan, Y. Zhang, N. Yang, Y. Li and Q. Chen, Development of encapsulation strategies towards the commercialization of perovskite solar cells, *Energy Environ. Sci.*, 2022, **15**, 13–55, DOI: 10.1039/D1EE02882K.

8 Y. H. Kim, H. Cho, J. H. Heo, T. S. Kim, N. S. Myoung, C. L. Lee, *et al.*, Multicolored Organic/Inorganic Hybrid Perovskite Light-Emitting Diodes, *Adv. Mater.*, 2015, **27**, 1248–1254, DOI: 10.1002/ADMA.201403751.

9 L. Dou, Y. M. Yang, J. You, Z. Hong, W. H. Chang, G. Li, *et al.*, Solution-processed hybrid perovskite photodetectors with high detectivity, *Nat. Commun.*, 2014, **5**, 1–6, DOI: 10.1038/ncomms6404.

10 A. Kojima, K. Teshima, Y. Shirai and T. Miyasaka, Organometal halide perovskites as visible-light sensitizers for photovoltaic cells, *J. Am. Chem. Soc.*, 2009, **131**, 6050–6051, DOI: 10.1021/JA809598R/SUPPL_FILE/JA809598R_SI_001.

11 M. Ameri, M. Ghaffarkani, R. T. Ghahrizjani, N. Safari and E. Mohajerani, Phenomenological morphology design of hybrid organic–inorganic perovskite solar cell for high efficiency and less hysteresis, *Sol. Energy Mater. Sol. Cells*, 2020, **205**, 110251, DOI: 10.1016/J.SOLMAT.2019.110251.

12 T. Xiang, Y. Zhang, H. Wu, J. Li, L. Yang, K. Wang, *et al.*, Universal defects elimination for high performance thermally evaporated $CsPbBr_3$ perovskite solar cells, *Sol. Energy Mater. Sol. Cells*, 2020, **206**, 110317, DOI: 10.1016/J.SOLMAT.2019.110317.

13 Australian manufacturer achieves 32% efficiency for inorganic perovskite solar cell – pv magazine Australia n.d. https://www.pv-magazine-australia.com/2022/10/18/australian-manufacturer-achieves-32-efficiency-for-inorganic-perovskite-solar-cell/accessed October 18, 2022.

14 H. Bi, G. Han, M. Guo, C. Ding, H. Zou, Q. Shen, *et al.*, Multistrategy Preparation of Efficient and Stable Environment-Friendly Lead-Based Perovskite Solar Cells, *ACS Appl. Mater. Interfaces*, 2022, **14**, 35513–35521, DOI: 10.1021/ACSAMI.2C06032/SUPPL_FILE/AM2C06032_SI_006.MP4.

15 K. Shivesh, I. Alam, A. K. Kushwaha, M. Kumar and S. V. Singh, Investigating the theoretical performance of Cs_2TiBr_6-based perovskite solar cell with La-doped $BaSnO_3$

and $CuSbS_2$ as the charge transport layers, *Int. J. Energy Res.*, 2022, **46**, 6045–6064, DOI: 10.1002/ER.7546.

16 Z. Shi, J. Guo, Y. Chen, Q. Li, Y. Pan, H. Zhang, *et al.*, Lead-Free Organic–Inorganic Hybrid Perovskites for Photovoltaic Applications: Recent Advances and Perspectives, *Adv. Mater.*, 2017, **29**, 1605005, DOI: 10.1002/ADMA.201605005.

17 M. I. Ustinova, S. D. Babenko, S. Y. Luchkin, F. S. Talalaev, D. v. Anokhin, S. Olthof, *et al.*, Experimental evaluation of indium(I) iodide as a lead-free perovskite-inspired material for photovoltaic applications, *J. Mater. Chem. C*, 2022, **10**, 3435–3439, DOI: 10.1039/D1TC05583F.

18 L. Romani, A. Speltini, C. N. Dibenedetto, A. Listorti, F. Ambrosio, E. Mosconi, *et al.*, Experimental Strategy and Mechanistic View to Boost the Photocatalytic Activity of $Cs_3Bi_2Br_9$ Lead-Free Perovskite Derivative by gC_3N_4 Composite Engineering, *Adv. Funct. Mater.*, 2021, **31**, 2104428, DOI: 10.1002/ADFM.202104428.

19 K. Ahmad, M. Q. Khan, R. A. Khan and H. Kim, Numerical simulation and fabrication of Pb-free perovskite solar cells ($FTO/TiO_2/Cs_3Bi_2I_9$/spiro-MeOTAD/Au), *Opt. Mater.*, 2022, **128**, 112458, DOI: 10.1016/J.OPTMAT.2022.112458.

20 S. L. Hamukwaya, H. Hao, M. M. Mashingaidze, T. Zhong, S. Tang, J. Dong, *et al.*, Potassium Iodide-Modified Lead-Free $Cs_3Bi_2I_9$ Perovskites for Enhanced High-Efficiency Solar Cells, *Nanomaterials*, 2022, **12**, 3751, DOI: 10.3390/NANO12213751.

21 T. B. Song, T. Yokoyama, S. Aramaki and M. G. Kanatzidis, *ACS Energy Lett.*, 2017, **2**, 897.

22 T. Okano and Y. Suzuki, Gas-assisted coating of Bi-based $(CH_3NH_3)_3Bi_2I_9$ active layer in perovskite solar cells, *Mater. Lett.*, 2017, **191**, 77–79.

23 X. Zhang, G. Wu, Z. Gu, B. Guo, W. Liu, S. Yang, T. Ye, C. Chen, W. Tu and H. Chen, Active-layer evolution and efficiency improvement of $(CH_3NH_3)_3Bi_2I_9$-based solar cell on TiO_2-deposited ITO substrate, *Nano Res.*, 2016, **9**(10), 2921–2930.

24 C. Ran, Z. Wu, J. Xi, F. Yuan, H. Dong, T. Lei, X. He and X. Hou, Construction of Compact Methylammonium Bismuth Iodide Film Promoting Lead-Free Inverted Planar Heterojunction Organohalide Solar Cells with Open-Circuit Voltage over 0.8 V, *J. Phys. Chem. Lett.*, 2017, **8**(2), 394–400.

25 S. S. Mali, H. Kim, D.-H. Kim and C. Kook Hong, Anti-Solvent Assisted Crystallization Processed Methylammonium Bismuth Iodide Cuboids towards Highly Stable Lead-Free Perovskite Solar Cells, *ChemistrySelect*, 2017, **2**(4), 1578–1585.

26 A. Kulkarni, T. Singh, M. Ikegami and T. Miyasaka, Photovoltaic enhancement of bismuth halide hybrid perovskite by *N*-methyl pyrrolidone-assisted morphology conversion, *RSC Adv.*, 2017, **7**(16), 9456–9460.

27 T. Singh, A. Kulkarni, M. Ikegami and T. Miyasaka, Effect of Electron Transporting Layer on Bismuth-Based Lead-Free Perovskite $(CH_3NH_3)_3Bi_2I_9$ for Photovoltaic Applications, *ACS Appl. Mater. Interfaces*, 2016, **8**(23), 14542–14547.

28 M. Q. Lyu, J. H. Yun, M. L. Cai, Y. L. Jiao, P. V. Bernhardt, M. Zhang, Q. Wang, A. J. Du, H. X. Wang, G. Liu and L. Z. Wang, Organic–inorganic bismuth (III)-based material: a lead-free, air-stable and solution-processable light-absorber beyond organolead perovskites, *Nano Res.*, 2016, **9**(3), 692–702.

29 B. W. Park, B. Philippe, X. L. Zhang, H. Rensmo, G. Boschloo and E. M. J. Johansson, Bismuth Based Hybrid Perovskites $A_3Bi_2I_9$ (A: Methylammonium or Cesium) for Solar Cell Application, *Adv. Mater.*, 2015, **27**(43), 6806.

30 C. F. Lan, J. T. Luo, S. Zhao, C. Zhang, W. G. Liu, S. Z. Hayase and T. L. Ma, Effect of leadfree $(CH_3NH_3)_3Bi_2I_9$ perovskite addition on spectrum absorption and enhanced photovoltaic performance of bismuth triiodide solar cells, *J. Alloy. Compd.*, 2017, **701**, 834–840.

31 B. Ghosh, B. Wu, H. K. Mulmudi, C. Guet, K. Weber, T. C. Sum, S. Mhaisalkar and N. Mathews, Limitations of $Cs_3Bi_2I_9$ as Lead-Free Photovoltaic Absorber Materials, *ACS Appl. Mater. Interfaces*, 2018, **10**(41), 35000–35007.

32 F. Bai, Y. Hu, Y. Hu, T. Qiu, X. Miao and S. Zhang, Lead-free, air-stable ultrathin $Cs_3Bi_2I_9$ perovskite nanosheets for solar cells, *Sol. Energy Mater. Sol. Cells*, 2018, **184**, 15–21.

33 M. B. Johansson, H. M. Zhu and E. M. J. Johansson, Extended Photo-Conversion Spectrum in Low-Toxic Bismuth Halide Perovskite Solar Cells, *J. Phys. Chem. Lett.*, 2016, **7**(17), 3467–3471.

34 M. T. Islam, M. R. Jani, K. M. Shorowordi, Z. Hoque, A. M. Gokcek, V. Vattipally, *et al.*, Numerical simulation studies of $Cs_3Bi_2I_9$ perovskite solar device with optimal selection of electron and hole transport layers, *Optik (Stuttg)*, 2021, **231**, 166417, DOI: 10.1016/J.IJLEO.2021.166417.

35 A. Das, S. D. Peu, Md A. M. Akanda, M. M. Salah, Md. S. Hossain and B. K. Das, Numerical Simulation and Optimization of Inorganic Lead-Free $Cs_3Bi_2I_9$-Based Perovskite Photovoltaic Cell: Impact of Various Design Parameters, *Energies*, 2023, **16**(5), 2328, DOI: 10.3390/en16052328.

36 J. Shin, M. Kim, S. Jung, C. S. Kim, J. Park, A. Song, K.-B. Chung, S.-H. Jin, J. H. Lee and M. Song, Enhanced efficiency in lead-free bismuth iodide with post treatment based on a holeconductor-free perovskite solar cell, *Nano Res.*, 2018, **11**(12), 6283–6293.

37 B.-W. Park, B. Philippe, X. Zhang, H. Rensmo, G. Boschloo and E. M. J. Johansson, *Adv. Mater.*, 2015, **27**, 6806.

38 S. S. Shin, J. P. Correa Baena, R. C. Kurchin, A. Polizzotti, J. J. Yoo, S. Wieghold, M. G. Bawendi and T. Buonassisi, *Chem. Mater.*, 2018, **30**, 336.

39 S. M. Jain, D. Phuyal, M. L. Davies, M. Li, B. Philippe, C. De Castro, Z. Qiu, J. Kim, T. Watson, W. C. Tsoi, O. Karis, H. Rensmo, G. Boschloo, T. Edvinsson and J. R. Durrant, *Nano Energy*, 2018, **49**, 614.

40 E. T. McClure, M. R. Ball, W. Windl and P. M. Woodward, *Chem. Mater.*, 2016, **28**, 1348.

41 M. R. Filip, X. Liu, A. Miglio, G. Hautier and F. Giustino, *J. Phys. Chem. C*, 2018, **122**, 158.

42 F. Hao, C. C. Stoumpos, D. H. Cao, R. P. H. Chang and M. G. Kanatzidis, *Nat. Photonics*, 2014, **8**, 489.

43 B.-B. Yu, L. Xu, M. Liao, Y. Wu, F. Liu, Z. He, J. Ding, W. Chen, B. Tu, Y. Lin, Y. Zhu, Zhang, X. Zhang, W. Yao,

A. B. Djurišić, J.-S. Hu, Z. He, *et al.*, *Sol. RRL*, 2019, **3**, 1800290.

44 Z. Shi, J. Guo, Y. Chen, Q. Li, Y. Pan, H. Zhang, Y. Xia and W. Huang, *Adv. Mater.*, 2017, **29**, 1605005.

45 B. Suarez, V. Gonzalez-Pedro, T. S. Ripolles, R. S. Sanchez, L. Otero and I. Mora-Sero, *J. Phys. Chem. Lett.*, 2014, **5**, 1628.

46 C. Liu, W. Li, C. Zhang, Y. Ma, J. Fan and Y. Mai, *J. Am. Chem. Soc.*, 2018, **140**, 3825.

47 D. P. McMeekin, G. Sadoughi, W. Rehman, G. E. Eperon, M. Saliba, M. T. Hörantner, A. Haghighirad, N. Sakai, L. Korte, B. Rech, M. B. Johnston, L. M. Herz and H. J. Snaith, *Science*, 2016, **351**, 151.

48 W. J. Yin, Y. Yan and S.-H. Wei, *J. Phys. Chem. Lett.*, 2014, **5**, 3625.

49 B. B Yu, M. Liao, J. Yang, W. Chen, Y. Zhu, X. Zhang, T. Duan, W. Yao, S. H. Wei, Z. He, *et al.*, *J. Mater. Chem. A*, 2019, **7**, 8818–8825.

50 T. L. Hodgkins, C. N. Savory, K. K. Bass, B. L. Seckman, D. O. Scanlon, P. I. Djurovich, M. Thompson and B. Melot, Anionic Order and Band Gap Engineering in Vacancy Ordered Triple Perovskites, *Chem. Commun.*, 2019, **55**, 3164–3167.

51 K. M. McCall, C. C. Stoumpos, O. Y. Kontsevoi, G. C. B. Alexander, B. W. Wessels and M. G. Kanatzidis, *Chem. Mater.*, 2019, **31**(7), 2644–2650, DOI: **10.1021/acs.chemmater.9b00636**.

52 F. Jiang, D. Yang, Y. Jiang, T. Liu, X. Zhao, Y. Ming, B. Luo, F. Qin, J. Fan, H. Han, L. Zhang and Y. Zhou, Chlorine Incorporation-Induced Formation of the Layered Phase for Antimony-Based Lead-Free Perovskite Solar Cells, *J. Am. Chem. Soc.*, 2018, **140**(3), 1019–1027.

53 J. Li, Q. Yu, Y. He, C. C. Stoumpos, G. Niu, G. Trimarchi, H. Guo, G. Dong, D. Wang, L. Wang and M. G. Kanatzidis, $Cs_2PbI_2Cl_2$, All-Inorganic Two-Dimensional Ruddlesden-Popper Mixed Halide Perovskite with Optoelectronic Response, *J. Am. Chem. Soc.*, 2018, **140**(35), 11085–11090.

54 N. Leblanc, N. Mercier, L. Zorina, S. Simonov, P. A. Senzier and C. Pasquier, Large Spontaneous Polarization and Clear Hysteresis Loop of a Room-Temperature Hybrid Ferroelectric Based on Mixed-Halide $[BiI_3Cl_2]$ Polar Chains and Methylviologen Dication, *J. Am. Chem. Soc.*, 2011, **133**(38), 14924–14927.

55 P. Blaha, K. Schwarz, F. Tran, R. Laskowski, G. Madsen and L. D. Mark, *J. Chem. Phys.*, 2020, **152**, 07410130, DOI: **10.1063/1.5143061@jcp.2020.ESS202**.

56 J. P Perdew and A. Zunger, *Phys. Rev. B: Condens. Matter Mater. Phys.*, 1981, **23**, 5048–5079, DOI: **10.1103/PhysRevB.23.5048**.

57 J. P. Perdew, K. Burke and Y. Wang, *Phys. Rev. Lett.*, 1996, **54**, 16533, DOI: **10.1103/PhysRevB.54.16533**.

58 F. Tran and P. Blaha, *Phys. Rev. Lett.*, 2009, **102**, 226401, DOI: **10.1103/PhysRevLett.102.226401**.

59 E. Danladi, M. Kashif, A. Ichoja and B. B. Ayiya, *Trans. Tianjin Univ.*, 2022, **29**, 62–72, DOI: **10.1007/s12209-022-00343-w**.

60 R. Cheng, C. C. Chung, H. Zhang, F. Liu, W. T. Wang, Z. Zhou, S. Wang, A. . B. Djurišic and S. P. Feng, Tailoring Triple-Anion Perovskite Material for Indoor Light Harvesting with Restrained Halide Segregation and Record High Efficiency Beyond 36%, *Adv. Energy Mater.*, 2019, **1–8**, 1901980, DOI: **10.1002/aenm.201901980**.

61 M. K. A. Mohammed, Boosting Efficiency in Carbon Nanotube-Integrated Perovskite Photovoltaics, *Langmuir*, 2024, **40**(51), 27114–27125, DOI: **10.1021/acs.langmuir.4c04679**.

62 L. R. Karna, R. Upadhyay and A. Ghosh, All-inorganic perovskite photovoltaics for power conversion efficiency of 31%, *Sci. Rep.*, 2023, **13**, 15212, DOI: **10.1038/s41598-023-42447-w**.

63 P. Subudhi and D. Punetha, Pivotal avenue for hybrid electron transport layer-based perovskite solar cells with improved efficiency, *Sci. Rep.*, 2023, **13**, 19485, DOI: **10.1038/s41598-023-33419-1**.

64 S. Z. Haider, H. Anwar and M. Wang, *Semicond. Sci. Technol.*, 2018, **33**, 035001, DOI: **10.1088/1361-6641/aaa596**.

65 E. Danladi, P. M. Gyuk, N. N. Tasie, A. C. Egbugha, D. Behera, I. Hossain, I. M. Bagudo, M. L. Madugu and J. T. Ikyumbur, *Heliyon*, 2023, **9**, e16838, DOI: **10.1016/j.heliyon.2023.e16838**.

66 M. K. A. Mohammed, Optimizing non-toxic $(CH_3NH_3)_3Bi_2I_9$ perovskite solar cells by SCAPS-1D, *Phys. Scr.*, 2024, **99**, 125980, DOI: **10.1088/1402-4896/ad9221**.

67 F. Birch, Finite Elastic Strain of Cubic Crystals, *Phys. Rev.*, 1947, **71**, 809–824, DOI: **10.1103/PhysRev.71.809**.

68 S. Mehmood, Z. Ali, Y. T. Alharbi, S. Alderhami and L. Almanqur, Structural and Magneto-Elastic Properties of the Quadruple Perovskites $CaCu_3B_2Os_2O_{12}$ (B = Mn–Ni): The Heisenberg Model and DFT Study, *J. Electron. Mater.*, 2023, **52**(23), 5872–5883.

69 T. Y. Tang, X. H. Zhao, X. N. Wei, D. Y. Hu, L. K. Gao and Y. L. Tang, *J. J. Nanoelectron. Optoelectron.*, 2021, **16**, 1521–1527, DOI: **10.1166/jno.2021.3100**.

70 A. Kumar, A. Kumar, A. Kumar and N. Iram, Ab-initio study of hybrid perovskites $Cs_2AgGaCl_6$ for solar cells applications, *Hybrid Adv.*, 2024, **6**, 100197, DOI: **10.1016/j.hybadv.2024.100197**.

71 M. Kibbou, Z. Haman, N. Khossossi, I. Essaoudi and A. Ainane, Rajeev Ahuja, Mater, *Chem. Phys.*, 2023, **254**, 126978, DOI: **10.1016/j.matchemphys.2022.126978**.

72 H. A. R. Aliabad, S. M. Hosseini, A. Kompany, A. Youssefi and E. A. Kakhki, *Phys. Status Solidi B*, 2009, **246**, 1072, DOI: **10.1002/pssb.200844359**.

73 I. Ullah, G. Murtaza, R. Khenata, A. Mahmood, A. Yar, M. Muzammil, N. Amin and M. Seleh, *J. Electro. Mater.*, 2016, **45**, 3059–3068.

74 Y. Al-Douri, B. Merabet, H. Abid and R. Khenata, *Superlattices. Microstruct*, 2012, **51**, 404–411doi, DOI: **10.1016/j.spmi.2012.01.004**.

75 R. Yu, Q. Ruan, F. Xiao and X. Ming, First-principles study on the optoelectronic properties of the quasi-one-dimensional flexible semiconductor K_2PdPS_4I, *Res. Phys.*, 2023, **47**, 106396, DOI: **10.1016/j.rinp.2023.106396**.

76 M. Hariharan and R. D. Eithiraj, Comprehensive study on structural, electronic, optical, elastic, and transport

properties of natural mercury sulphohalides *via* DFT computation, *Sci. Report.*, 2024, **14**, 18593, DOI: **10.1038/s41598-024-69430-3**.

77 M. K. A. Mohammed, Efficient Perovskite Photovoltaics by a Nanostructured Ga_2O_3 Hole-Blocking Layer, *Energy Fuels*, 2024, **38**(7), 6387–6396, DOI: **10.1021/acs.energyfuels.4c00376**.

78 M. K. A. Mohammed, Boosting the performance of $CH_3NH_3PbI_3$ perovskite solar cells with a well-aligned polymeric hole-transporting layer, *Indian J. Phys.*, 2024, **98**, 1–10, DOI: **10.1007/s12648-024-03500-0**.

79 L. J. Bartolotti, S. R. Gadre and R. G. Parr, Electronegativities of the elements from simple. CHI. alpha. theory, *J. Am. Chem. Soc.*, 1980, **102**(9), 2945–2948, DOI: **10.1021/ja00529a013**.

80 K. Maeda, Photocatalytic water splitting using semiconductor particles: History and recent developments, *J. Photochem. Photobiol., C*, 2011, **12**, 237–268, DOI: **10.1016/j.jphotochemrev.2011.07.001**.

81 Z. Wang, J. Hong, S. F. Ng, W. Liu, J. Huang, P. Chen and W. J. Ong, Recent Progress of Perovskite Oxide in Emerging Photocatalysis Landscape: Water Splitting, CO_2 Reduction, and N_2 Fixation, *Acta Phys. Chim. Sin.*, 2021, **37**(6), 2011033, DOI: **10.3866/PKU.WHXB202011033**.

82 D. Feng, X. Li, Y. Liu, X. Chen and S. Li, Emerging Bismuth-Based Step-Scheme Heterojunction Photocatalysts for Energy and Environmental Applications, *Renewables*, 2023, **1**, 485–513, DOI: **10.31635/renewables.023.202300037**.